Excess $PbBr_2$ Passivation of Large PbS Colloidal Quantum Dots to Reduce Dark-Current Density for Near-Infrared Detection

Junrui Yang,[1,†] Shuaicheng Lu,[1,2,3,†] Bing Xia,[1] Peilin Liu,[1] Yang Yang,[1] Zewen Xiao,[1,2] Jianbing Zhang,[1,2,3] Liang Gao,[1,2,3,*] and Jiang Tang[1,2]

[1] *Wuhan National Laboratory for Optoelectronics (WNLO) and School of Optical and Electronic Information, Huazhong University of Science and Technology, 1037 Luoyu Road, Wuhan, People's Republic of China*

[2] *Optics Valley Laboratory, 1037 Luoyu Road, Wuhan, People's Republic of China*

[3] *Wenzhou Advanced Manufacturing Technology Research Institute of Huazhong University of Science and Technology, 225 Chaoyang New Street, Wenzhou, People's Republic of China*

(Received 29 July 2022; revised 22 October 2022; accepted 13 December 2022; published 6 January 2023)

Small-size PbS colloidal quantum dots (CQDs) have achieved excellent performance in photoelectric conversion devices through the ligand-exchange method of mixed lead-halide passivation. However, with the increase of PbS CQD diameter, the proportion of (100) facets on the CQD surface increases and the original proportion of mixed lead-halide ligand cannot passivate (100) facets completely, which will introduce deep defects and deteriorate device performance. Here, we demonstrate an excessive $PbBr_2$ concentration ligand strategy to sufficiently passivate large-size PbS CQDs with an absorption peak at 1300 nm. The first-principles calculation results suggest that Br^- can passivate (100) facets more efficiently compared with I^-. With the increase of $PbBr_2$ concentration (0–0.464 mmol/mL), both optical and electrical measurements imply that defects are effectively passivated, while carrier lifetime increases and dark-current density decreases. Finally, a device with specific detectivity of 5.22×10^{12} Jones is obtained. This passivation strategy can also be used in other large-size PbS CQDs (diameter >4 nm) to realize a better device performance.

DOI: 10.1103/PhysRevApplied.19.014021

I. INTRODUCTION

Colloidal quantum dots (CQDs) are widely used in photoelectric conversion devices due to their size-tunable band gap [1], multiple exciton generation [2], and large absorption coefficient [3]. Lead-sulfide (PbS) CQDs have attracted much attention due to their great potential for developing high-performance and low-cost near-infrared detection technology [4]. However, incomplete passivation of CQD surfaces results in interdots' fusion [5] and gap states [6,7], decreasing carrier lifetime [8,9], and degrading device performance [10,11]. Thus, deeply understanding the complex properties of (100) and (111) facets on the PbS CQD surface and exploring a suitable passivation method are essential for obtaining high-performance devices.

The ligand-exchange (LE) method is used in PbS CQDs' film-fabrication process to replace oleic acid molecules on CQDs' surface and passivate defect sites. The mixed ligand of high PbI_2 to $PbBr_2$ molar ratio (>5:1) is the most common ligand used in small-size PbS CQD passivation. For the small-size PbS CQDs whose diameters are below 4 nm (band gap >1.06 eV), the CQD surfaces are mainly composed of (111) facets. Plenty of I^- ions passivate (111) facets, while a few of Br^- ions passivate (100) facets and suppress fusions [5,12,13]. When the diameter of PbS CQD increases to 4.61 nm (band gap approximately 0.95 eV), the proportion of (100) facets rises to 22.4% [14]. The traditional mixed ligand used for small-size PbS CQDs could not sufficiently passivate (100) facets, resulting in fusion between CQDs and trap states [6,15]. Therefore, sufficient passivation of (100) facets is vital for large-size PbS CQDs to reduce the density of trap states and achieve high-performance devices.

Here, we report a mixed halide ligand of high PbI_2 and high $PbBr_2$ to sufficiently passivate 1300 nm PbS CQDs ($E_g = 0.96$ eV), which significantly reduces the defect density and dark-current density of photodetector devices. The first-principles calculation results suggest that Br^- has a lower adsorption energy compared with I^-, and can passivate (100) facets more efficiently. The dark-current density of the optimal device passivated by high $PbBr_2$ concentration ligand at −0.1 V decreases to 156 nA/cm^2 in contrast to the 11.3 ± 3.8 $\mu A/cm^2$ of low $PbBr_2$ concentration ligand. Finally, a device with specific detectivity of 5.22×10^{12} Jones is obtained, which demonstrates a superior performance among large-size PbS CQD photodetectors.

*highlight@hust.edu.cn

†These authors contributed equally to this work.

II. RESULTS AND DISCUSSION

A. Theoretical calculation of (100) surfaces

Halide ligand can bind with Pb dangling bonds on the PbS CQDs' (100) facets at top and bridge sites. To investigate the passivation effect of Br^- and I^- on (100) facets, we calculate the adsorption energy of Br^- and I^- at top and bridge sites by a slab model in Figs. 1(a) and 1(b) [16,17]. The related density-functional theory (DFT) simulations are accomplished based on methods in Refs. [18–22]. An ion with lower adsorption energy is easier to adsorb on the surface. Adsorption of Br^- and I^- at bridge sites (−0.67 eV/ion and −0.36 eV/ion) is stronger than at top sites (−0.61 eV/ion and −0.28 eV/ion), indicating a more stable binding at bridge sites.

We further calculate the adsorption energy and bond length of Br^- and I^- at bridge sites varied with the atom coverage of 1, 2, 4, 6, 8, and 10. Because the interaction between halide ligands restrains the adsorption of more atoms, the adsorption energy increases with the atom coverage from 1 to 8. Meanwhile, Br^- has lower adsorption energy compared with I^- at the same atom coverage, indicating the more excellent ability of Br^- on passivating (100) facets than I^- [Fig. 1(e)]. However, Pb atoms are obviously pulled out from (100) facets at the atom coverage of 8 [Figs. 1(c) and 1(d)]. When the atom coverage of Br^- up to 10, the dislocation of Pb atoms due to the binding between Br and Pb would damage the structure of (100) facets [23]. In this case, extremely excessive Br^- would damage (100) facets and introduce defects.

Besides, we calculate the bond length of Pb—Br and Pb—I varied with atom coverage [Fig 1(f)]. With the increase of atom coverage, the bond length of Pb—Br decreases while bond length of Pb—I increases, indicating a tighter bond of Br^- on (100) facets at high atom coverage than in the case of I^-. In conclusion, choosing an appropriate Br^- concentration is necessary to obtain high-performance PbS CQD detectors.

B. Optical characterization of PbS CQD films

Then we fabricate PbS CQD films by a ligand-exchange method [24]. The pristine PbS CQDs are synthesized and washed based on a previously reported method [25]. We change the concentration of $PbBr_2$ in N, N-dimethylformamide (DMF): 0.029 mmol/mL (1 × $PbBr_2$), 0.116 mmol/mL (4 × $PbBr_2$), 0.232 mmol/mL (8 × $PbBr_2$), and 0.464 mmol/mL (16 × $PbBr_2$) with a fixed PbI_2 concentration (0.266 mmol/mL). To understand the effect of different $PbBr_2$ concentrations on CQD films, we characterize the optical properties of CQD films.

Figure 2(a) shows the normalized absorption spectra measured from 0.73 to 1.13 eV (1100 to 1700 nm). 1 × $PbBr_2$, 4 × $PbBr_2$, and 8 × $PbBr_2$ films show similar absorption peak position and shape, but 16 × $PbBr_2$ film shows a slight blueshift of peak position. Higher-concentration $PbBr_2$ treated PbS CQD films are filled with higher molar concentration of $PbBr_2$ and PbI_2 [27,28], which leads to longer interdot space. The blueshift of the peak position is possibly caused by the reduced CQD coupling due to the longer interdot space [29].

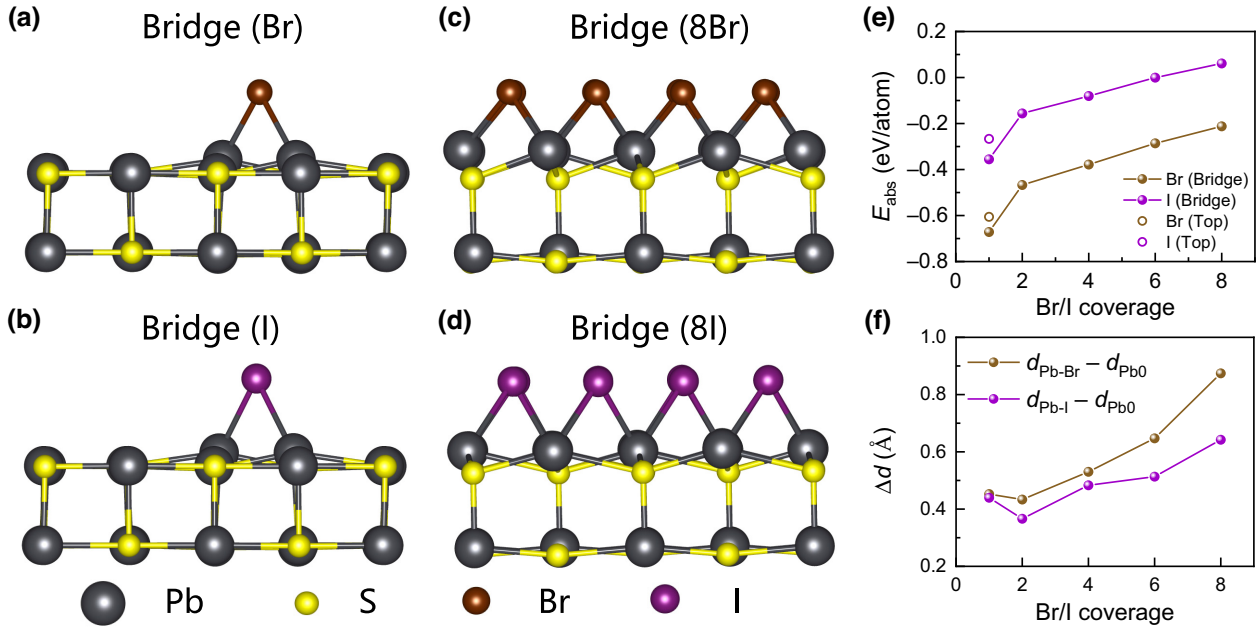

FIG. 1. Schematic diagram of PbS CQD (100) facets passivated by (a) 1 Br^-, (b) 1I^-, (c) 8Br^-, and (d) 8I^-. (e) Adsorption energy of Br^- and I^- on different sites varied with atom coverage. (f) Bond length of Pb—I and Pb—Br varied with atom coverage.

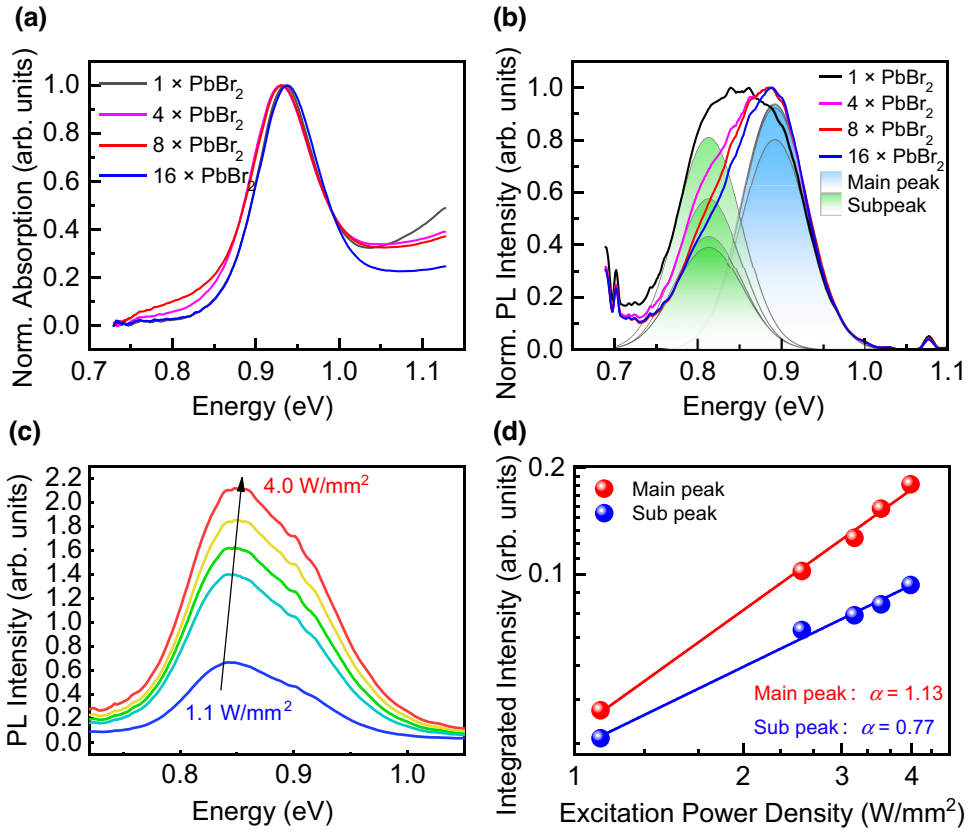

FIG. 2. (a) Absorption and (b) PL spectra of PbS CQD films passivated by different concentrations of Br^-. (c) Excitation power-dependent PL of 1 × $PbBr_2$ PbS CQD film. (d) Excitation power-dependent PL intensity of the exciton transition (approximately 0.891 eV) peak and the trap-related transition (approximately 0.813 eV) peak. Solid lines: power-law fit. The absorption and PL spectra are converted from wavelength to energy scale by using a Jacobian matrix transformation [26].

Figure 2(b) shows the normalized PL spectra excited by a 980-nm laser. The PL spectra are comprised of two peaks. Therefore, we perform peak splitting of PL spectra and recorded the variation of two peaks [Fig. 2(b) and Table I]. The main peak at 0.892 eV corresponds to the absorption spectra at 0.930 eV with a Stokes shift, resulting from carrier transition between the conduction band and the valence band. The subpeak at 0.813 eV corresponds to carrier transition between gap states and free states (conduction band or valence band). With $PbBr_2$ concentration increasing from 1 × $PbBr_2$ to 16 × $PbBr_2$, the integrated intensity of the subpeak decreases from 0.0795 to 0.0400. Therefore, higher concentration of Br^- effectively reduces gap states of PbS CQDs, consistent with the theoretical calculation results. Besides, the subpeak intensities difference between 8 × $PbBr_2$ and 16 × $PbBr_2$ films is lower than the difference between 1 × $PbBr_2$ and 4 × $PbBr_2$ films, resulting from the passivation saturation of Br^- mentioned in theoretical calculation.

To explore the transitions of two peaks more deeply, we characterize the excitation power-dependent PL spectra of 1 × $PbBr_2$ films [Fig. 2(c)], and perform a peak splitting [30]. The relationship between excitation power and integrated PL intensity is expressed as

$$I_{\mathrm{PL}} \propto I_{\mathrm{ex}}^{\alpha} \tag{1}$$

TABLE I. PL peak-splitting data of PbS CQD films passivated with different concentrations of $PbBr_2$.

Film	Position 1 (eV)	Area 1	FWHM 1 (eV)	Position 2 (eV)	Area 2	FWHM 2 (eV)	Stokes shift (eV)
1 × $PbBr_2$	0.892	0.0797	0.0794	0.813	0.0795	0.0783	0.043
4 × $PbBr_2$	0.892	0.0890	0.0770	0.813	0.0553	0.0766	0.038
8 × $PbBr_2$	0.892	0.0935	0.0795	0.813	0.0430	0.0793	0.039
16v$PbBr_2$	0.892	0.0895	0.0765	0.813	0.0400	0.0816	0.046

for exciton transitions, $1 < \alpha < 2$, while $0 < \alpha < 1$ for trap-related transition [31,32]. We fit excitation power-dependent PL intensity with Eq. (1) and obtain $\alpha_{\text{subpeak}} = 0.77$, $\alpha_{\text{mainpeak}} = 1.13$ [Fig. 2(d)]. Therefore, the main peak at 0.892 eV results from exciton transition, and trap-related transition results in the subpeak at 0.813 eV.

We also calculate Stokes shifts of CQD films using the original PL and absorption data (Table I). $4 \times PbBr_2$ and $8 \times PbBr_2$ films have smaller Stokes shifts (0.038 and 0.039 eV) compared to $1 \times PbBr_2$ film (0.043 eV), indicating $4 \times PbBr_2$ and $8 \times PbBr_2$ films have a smaller density of gap states than $1 \times PbBr_2$ film. However, the Stokes shift of $16 \times PbBr_2$ film (0.046 eV) is bigger than that of $8 \times PbBr_2$ film (0.039 eV) due to the above-mentioned absorption peak blueshift.

C. Electrical characterization of PbS CQD devices

We further prepare photodiode devices to investigate the influence of different concentrations of $PbBr_2$ passivation on device performance. The devices are fabricated on ITO electrodes. Firstly, we fabricate 200-nm ZnO as the electron transport layer by rf sputtering on ITO glass substrate. Secondly, we spin-coated 400-nm absorption layer PbS CQDs passivated by different concentrations of $PbBr_2$ and a fixed PbI_2 on ZnO in nitrogen. We then spin-coated 50-nm hole-transport layer of PbS CQDs capped with 1, 2-ethanedithiol ligands (PbS-EDT) by the layer-by-layer method. Finally, 120-nm patterned Au electrodes are evaporated on the top of the PbS-EDT layer. Figure 3(a) shows the structure schematic of PbS CQD devices. The cross-section scanning electron microscopy (SEM) image and detailed energy band structure of the PbS CQD device are shown in Ref. [33].

Firstly, we characterize the current density-voltage (J-V) curves of the devices passivated by different concentrations of $PbBr_2$ [34]. With the concentration increasing from $1 \times PbBr_2$ to $16 \times PbBr_2$, the dark-current density (J_{dark}) of devices at -0.1 V decreases from 11.3 ± 3.8 μA/cm^2 to 182 ± 37 nA/cm^2, and then increases to 362 ± 109 nA/cm^2 [Fig. 3(b)], while external quantum efficiency (EQE) at 1300 nm increases from $19.6 \pm 0.9\%$ to $21.6 \pm 1.3\%$, and then decreases to $12.7 \pm 1.9\%$ [Fig. 3(c) and Table II]. We used Eq. (2) to analyze typical dark J-V curves of devices passivated by different concentrations of $PbBr_2$ based on the circuit model demonstrated in Ref. [35]. The dark current is comprised of the diode current, the Ohmic leakage current caused by leakage sites, and the trap-assisted tunneling leakage current caused by interface defects [36,37].

$$J = J_0\{\exp[q(V - J \times R_s)/nkT] - 1\} + (V - J \times R_s)/R_{\text{sh}} + kV\exp[m/(V - V_{\text{bi}})] \quad (2)$$

V and J in Eq. (2) are applied bias and output current density. J_0 is the reverse saturation current density, determined by carrier lifetime, depletion width, and carrier concentration. R_s and R_{sh} are the device series resistance and shunt resistance; n is the diode quality factor; k and m are related to defect level and concentration at the interface.

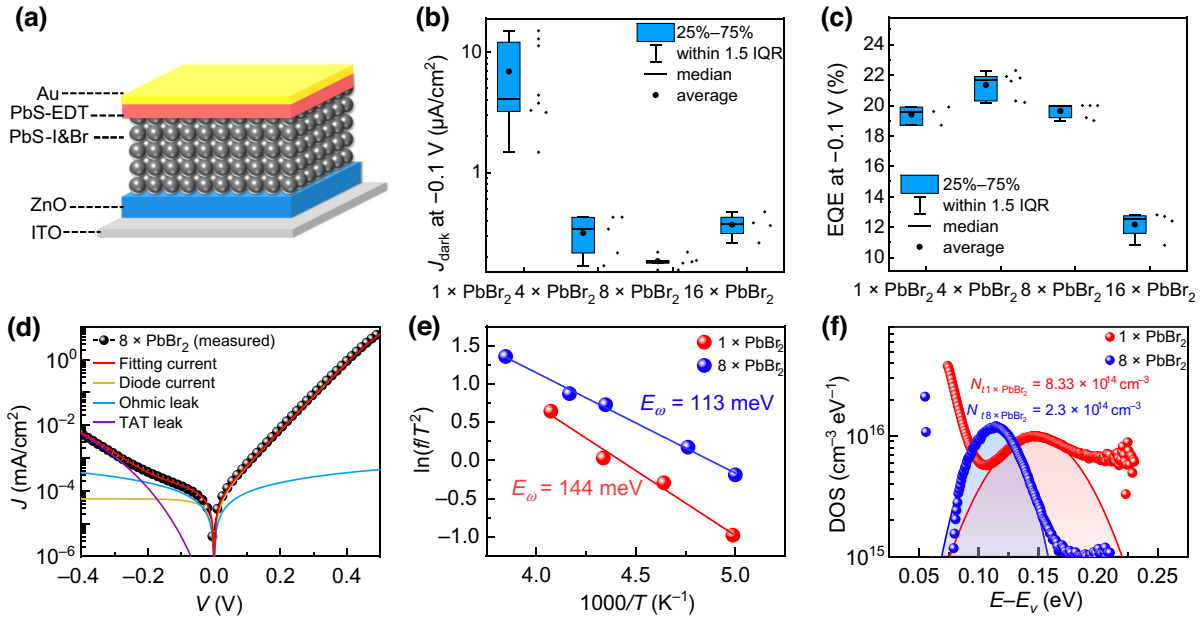

FIG. 3. (a) Structure schematic of PbS CQD devices. (b) Dark-current density and (c) EQE at -0.1 V of devices passivated by $1 \times PbBr_2$, $4 \times PbBr_2$, $8 \times PbBr_2$, and $16 \times PbBr_2$. (d) Dark J-V curve fitting of the $8 \times PbBr_2$ device. (e) The Arrhenius plot of $\ln(f/T^2)$ of the maxima of fdC/df and (f) DOS distribution of $8 \times PbBr_2$ device (blue) and $1 \times PbBr_2$ device (red).

TABLE II. Dark-current density and EQE at −0.1 V of PbS CQD devices passivated with different concentrations of $PbBr_2$.

Device	J_{dark} (μA/cm^2)	EQE (%)
1 × $PbBr_2$	11.3 ± 3.8	19.6 ± 0.9
4 × $PbBr_2$	0.34 ± 0.124	21.6 ± 1.3
8 × $PbBr_2$	0.18 ± 0.037	19.2 ± 0.8
16 × $PbBr_2$	0.36 ± 0.109	12.7 ± 1.9

Parameters obtained after curve fitting are shown in Table III. With the increasing concentration of $PbBr_2$, J_0 decreases gradually from 5×10^{-4} mA/cm^2 to 3.97×10^{-5} mA/cm^2. To understand the variation of J_0, we characterize temperature-dependent admittance spectroscopy (TDAS) of 1 × $PbBr_2$ and 8 × $PbBr_2$ devices [Figs. 3(e) and 3(f)]. The 8 × $PbBr_2$ device has narrower defect distribution and shallower defect level compared with the 1 × $PbBr_2$ device, showing that moderate Br^- passivate CQD defects more effectively. We also characterize transient absorption spectra (TAS) [38,39] and calculate carrier lifetime based on a method used in Refs. [40–42], showing that 8 × $PbBr_2$ film has a longer carrier lifetime than 1 × $PbBr_2$ film. Therefore, the decreased J_0 is due to the increased carrier lifetime caused by the defect passivation of Br^-.

We also find that the ideality factor n decreased at first and then increased. The ideality factor n describes the quality of p-n junction. Junction current can be further divided into generation-recombination current (J_{GR}) and diffusion current (J_{diff}). Generally, n ($1 < n < 2$) evaluates the proportion of J_{diff} in junction current. Devices with lower n have a lower proportion of J_{diff}, a higher proportion of J_{GR}, lower dark-current density and better device performance. To analyze factors affecting n, we use the J_{GR}/J_{diff} to characterize the proportion of GR current and diffusion current, and J_{GR}/J_{diff} is positively correlated to n. For an N^+P junction, J_{GR}/J_{diff} is expressed as Eq. (3):

$$J_{GR}/J_{diff} \propto \left[N_D W/\left(2n_i\sqrt{\mu\tau}\right)\right], \tag{3}$$

where N_D is the doping density, W is the width of depletion region, n_i is the intrinsic carrier concentration, μ is the mobility, τ is the carrier lifetime. From 1 × $PbBr_2$ to 8 × $PbBr_2$ devices, τ increases due to defect passivation, resulting in the decrease of J_{GR}/J_{diff} and n. The carrier mobility (μ) of CQD film could be described by hopping mode and proportional to the tunneling rate [29,43,44]. Along with the increase of $PbBr_2$, the interdot space increases, leading to wider tunneling barrier and lower μ. Decreased μ leads to the decrease of J_{GR}/J_{diff} and n while increased τ results in increased J_{GR}/J_{diff} and n. Therefore, n exists a minimum with the $PbBr_2$ concentration, which can be attributed to the balance between carrier mobility and lifetime.

The atomic force microscope (AFM) images [45] reveal that CQD films with higher concentration of Br^- are smoother with fewer cracks serving as the leakage channel, corresponding to the variation of R_{sh}. The x-ray photoelectron spectroscopy (XPS) results show that CQD film with higher concentration of Br^- has lower carbon content, meaning more sufficient ligand exchange [36,46]. The 1 × $PbBr_2$ film has a lot of cracks caused by solvent evaporation and organic ligand removal, resulting in detrimental shunt path and a decrease in R_{sh} [47–49].

For reverse bias, we induce the trap-assisted tunneling (TAT) current model [36]. k and m are parameters of trap-assisted tunneling current, respectively, related to the trap density and energy level. When the bias ranged from −0.4 to −0.2 V, the J_{dark} is dominated by TAT current density [Fig. 3(d)]. Devices passivated by higher concentration of $PbBr_2$ have the same k and smaller m, indicating the passivation of interface traps in higher $PbBr_2$ concentration devices.

D. Comprehensive performance characterization of the best PbS CQD devices

We then characterize the detection performance of the best device (8 × $PbBr_2$). Figure 4(a) shows the response of the device to 590-nm light varied with frequency. The 590-nm light-emitting diode (LED) source is modulated by sine wave to ensure that the frequency spectra of input signal corresponds to one frequency. The −3-dB bandwidth of the 8 × $PbBr_2$ device at zero bias is 38 kHz. Figure 4(b) shows the wavelength-dependent EQE measured at −0.1 V bias. The 8 × $PbBr_2$ device generates an EQE of 22.78% at 1300 nm. Figure 4(c) shows the response of the 8 × $PbBr_2$ device illuminated by 1300-nm light with different power density. Linear dynamic range (LDR) defines

TABLE III. Fitting data of typical dark J-V curves of PbS CQD devices passivated with different concentrations of $PbBr_2$.

Device	J_0 (mA/cm^2)	n	R_{sh} (Ω cm^2)	R_s (Ω cm^2)	k (1/Ω)	m (V)
1 × $PbBr_2$	5×10^{-4}	1.796	10	0.002	NA	NA
4 × $PbBr_2$	9.4×10^{-5}	1.58	400	0.002	5.37	4.7
8 × $PbBr_2$	4.6×10^{-5}	1.55	1122	0.003	5.37	4.4
16 × $PbBr_2$	3.97×10^{-5}	1.92	780	0.072	5.37	4.1

NA, not available.

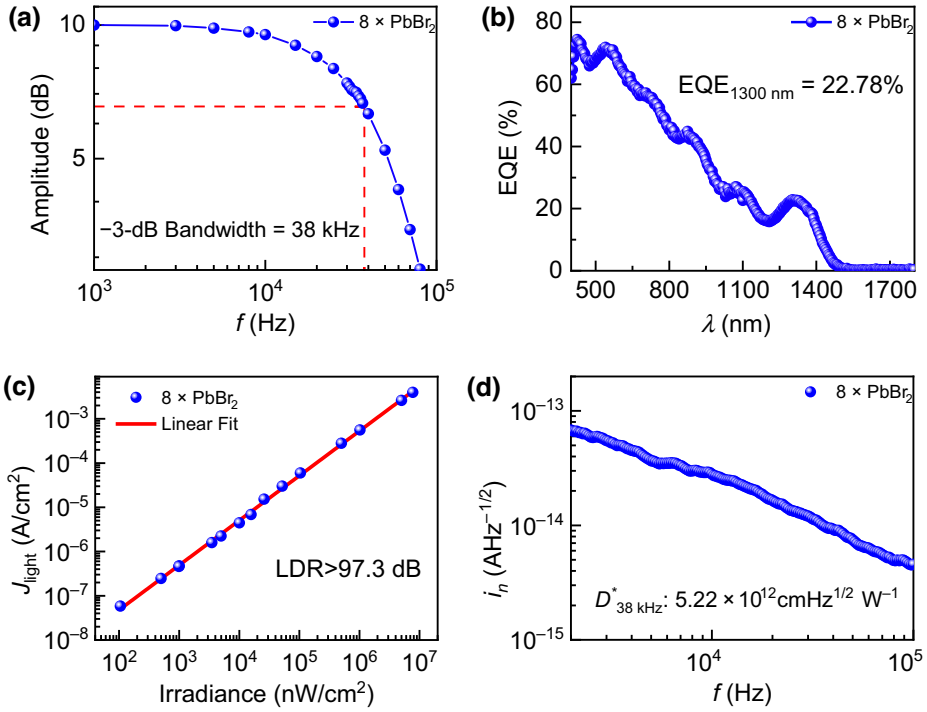

FIG. 4. (a) Frequency response of 8 × $PbBr_2$ device at zero bias. (b) Wavelength-dependent EQE of 8 × $PbBr_2$ device at −0.1 V bias. (c) Photocurrent density of 8 × $PbBr_2$ device at zero bias illuminated by different-power irradiance. (d) Noise power density of 8 × $PbBr_2$ device at zero bias.

the range in which photocurrent varies linearly with incident power density. The LDR of the 8 × $PbBr_2$ device at zero bias is over 97.3 dB.

To quantify the detection efficiency of the best device, we calculate the specific detectivity D^* of the device using the following equation:

$$D^* = R\sqrt{A\Delta f}/i_n, \tag{4}$$

where R is the responsivity calculated from EQE at 1300 nm, A is the area of the electrode (0.0706 cm^2), Δf is the bandwidth of the measurement circuit, and i_n is the noise current. The noise power density is measured by the lock-in amplifier setting the circuit bandwidth as 1 Hz. Figure 4(d) shows the noise power density $\left(i_n/\sqrt{\Delta f}\right)$ of the best device (8 × $PbBr_2$) device at zero bias. We choose the noise power density at −3-dB bandwidth and get the D^* of 5.22×10^{12} Jones. Compared with previous PbS CQD photodetectors, our optimal PbS CQD photodiode shows an excellent performance in sensitivity [50–56].

III. CONCLUSION

In summary, we develop an excessive concentration of $PbBr_2$ ligand strategy to solve the insufficient passivation issue of (100) facets on the large-size PbS CQD surface. This method effectively suppresses defects and increases carrier lifetime. Meanwhile, continuing to increase the $PbBr_2$ concentration decreases the EQE due to the hindrance of carrier transport by too thick $PbBr_2$. As a result, a balance between carrier transport and defect passivation of (100) facets could be achieved with the application of 0.232 mmol/mL $PbBr_2$ (8 × $PbBr_2$) in ligand exchange. This finally generates the minimum dark-current density of 156 nA/cm^2 at −0.1 V and a specific detectivity of 5.22×10^{12} Jones. This simple and efficient approach should also contribute to the passivation of other large-size PbS CQDs (diameter >4 nm) and obtain high-performance infrared photodetectors.

ACKNOWLEDGMENTS

The authors gratefully acknowledge financial support from the National Key Research and Development Program of China (No. 2021YFA0715502), the National Natural Science Foundation of China (No. 61904065), Key R & D program of Hubei Province (2021BAA014), International science and technology cooperation project of Hubei Province (2021EHB010), the fund for Innovative Research Groups of the Natural Science Foundation of Hubei Province (No. 2020CFA034), Scientific Research Project of Wenzhou (G20210013), and the China Postdoctoral Science Foundation (No. 2021M691118, 2022M711237). The authors also thank the TA test support of Professor Guijie Liang and Gaoyuan Yang, and the Analytical and Testing

Center of Huazhong University Science and Technology for the characterization.

APPENDIX: METHODS

1. DFT simulations

DFT simulations are accomplished by the projector augmented-wave (PAW) method [18], which is applied in the Vienna *ab initio* simulation package (VASP).[19] The general gradient approximation (GGA) Perdew-Burke-Ernzerhof (PBE) function [20] is used for all the structural relaxations. The plane-wave cutoff energy is set to 500 eV for all calculations. PbS{100}/Br and PbS{100}/I systems with five atomic layers in total and a vacuum layer of 15 Å are used for interface calculations. Γ-centered Monkhorst-Pack [21] meshes sized $4 \times 4 \times 1$ (PbS{100}/Br or I system) are employed for sampling the Brillouin zones, and the corresponding atom positions are relaxed until the total force on each atom is less than 0.02 eV $Å^{-1}$. The crystal-structure diagram is created by VESTA [22].

The adsorption energy E_{ads} is widely used to characterize the strength of adsorption capacity and the stability of adsorption structure, and E_{ads} could be determined by the following definitions:

$$nE_{ads} = E_{slab\text{-}x} - (E_{slab} + nE_x),$$

where n is the number of adsorption atoms, E_x is the energy of single adsorption atom, E_{slab} is the bare slab energy, and $E_{slab\text{-}x}$ is the energy of slab after atom adsorption. Adsorption energy (E_{ads}) calculated from this equation is minus, and the atom with a higher absolute value of E_{ads} has a stronger adsorption ability.

2. Chemicals

Lead chloride ($PbCl_2$, 99.99%), lead iodide (PbI_2, 99.99%), lead bromide ($PbBr_2$, 99.99%), oleylamine (OLA, > 80%), n-octylamine (99%), N,N-dimethylformamide (DMF, 99.8%) and n-butylamine (BTA, 99%) are purchased from Aldrich and used as received. Oleic acid (OA, 90%), 1-octadecene (ODE, 90%), and zinc stearate (>12.5%) are purchased from Alfa and used as received. Hexane (97%) and ethanol (99.7%) are acquired from Greagent and acetone from Sinopharm.

3. CQD synthesis and ligand exchange

The PbS CQDs are synthesized and washed based on a previously reported method [25]. We carry out the ligand-exchange process in the solution phase in a N_2-filled glove box. Firstly, the exchange solution is carefully prepared by dissolving lead iodide (PbI_2, 0.266 mmol/mL), and different concentrations of lead bromide ($PbBr_2$) in N, N-dimethylformamide (DMF). Then, CQD solution in octane (10 mg/ml) is added into the exchange solution at a 1:1 volume ratio. Then, the mixed solution is shaken vigorously for 30 s until CQDs are completely transferred to the DMF phase. The DMF solution is then washed 2 times using octane with the same volume of DMF. After the exchange process, CQDs are then separated by centrifugation. This is followed by a vacuum-drying process for 40 min.

4. CQD film fabrication

The vacuum-dried CQDs are redispersed in a mixed solvent of 4:1 (volume ratio) N-butylamine (BTA) and DMF with 300 mg/ml. The hybrid ink is deposited by spin coating at 2500 rpm for 40 s to achieve an optimized thickness. This is followed by a 10-min 90 °C annealing process to remove solvent residues.

5. Device fabrication

The devices are fabricated on 2.5×2.5 cm^2 glass substrates covered by 1×2.5 cm^2 striped indium-doped tin-oxide (ITO) electrodes bought from Youxuan Tech. Firstly, we fabricate 200-nm electron transport layer zinc oxide (ZnO) by rf sputtering. The sputtering target is zinc oxide of 99.9% purity from Zhongnuo New Material Company. The typical parameter of ZnO sputtering is as follows: sample substrate kept at 25 °C, sputtering power density of 4.38 W/cm^2, mixture of argon and oxygen with a V_{Ar2} : V_{O2} ratio of 99:1, chamber pressure is 0.55 pa measured by Pirani gauge during sputtering. The PL spectrum and XRD pattern of ZnO film are shown in Ref. [57]. Secondly, we spin coat 400-nm absorption layer PbS CQDs passivated by different concentrations of Br^- on ZnO in nitrogen. We then spin coat two layers of CQDs (first exciton peak at 880 nm) that are treated with EDT ligand (0.01% volume EDT-acetonitrile solution) as the hole transport layer (PbS-EDT). Finally, 80-nm patterned Au electrodes are thermally evaporated on the top of the PbS-EDT layer. The electrode area of the prepared PbS CQD device is 0.0706 cm^2.

6. Film and device characterizations

The PL spectra are excited by a 980-nm laser with power densities of 1.1, 2.6, 3.2, 3.5, and 4.0 W/mm^2 and obtained by a QuantaMaster 8000 steady-state transient modular fluorescence spectrometer. The optical absorption spectra are measured by a SolidSpec-3700 ultraviolet-visible-near-infrared spectrophotometer. The SEM images are acquired by GeminiSEM 300 field-emission scanning electron microscope. The XPS spectra are excited by Al Kα x ray (1486.6 eV) and collected using an AXIS-ULTRA DLD-600W x-ray photoelectron spectrometer. The binding energy scale of XPS is calibrated by measuring the binding energy of C 1 s (285.000 eV). Transient absorption (TA) spectra are carried out by Ultrafast System Helios Fire, which includes an 85-fs pump laser at 750 nm with a power of 5 μW, a repetition frequency of 1000 Hz,

a spot size of 0.059 mm^2, and a Femto-TA spectrometer as a probe system. The *J-V* curves are tested by an Agilent B1500A semiconductor characterization system. The −3-dB bandwidth measurements are performed with a Thorlabs LED modulated by a function generator (Agilent 33210A) and a lock-in amplifier (Stanford Research Systems, SR850). The noise power spectra are performed with a preamplifier (Stanford Research Systems, SR570) and a lock-in amplifier (Stanford Research Systems, SR850). The LDR is measured under a 1300-nm LED (Thorlabs) with a tunable power density by changing the LED current and distance between LED and devices. The power density (from 105 nW/cm^2 to 7.7 mW/cm^2) are calibrated by a 1×1 cm^2 optical power meter (PM101, Thorlabs) at the same position of the measured device. The AFM images are measured by a scanning probe microscope (SPM-9700, Shimadzu, Japan).

[1] E. M. Miller, D. M. Kroupa, J. Zhang, P. Schulz, A. R. Marshall, A. Kahn, S. Lany, J. M. Luther, M. C. Beard, C. L. Perkins, and J. van de Lagemaat, Revisiting the valence and conduction band size dependence of PbS quantum dot thin films, ACS Nano **10**, 3302 (2016).

[2] A. J. Nozik, M. C. Beard, J. M. Luther, M. Law, R. J. Ellingson, and J. C. Johnson, Semiconductor quantum dots and quantum dot arrays and applications of multiple exciton generation to third-generation photovoltaic solar cells, Chem. Rev. **110**, 6873 (2010).

[3] C. A. Leatherdale, W. K. Woo, F. V. Mikulec, and M. G. Bawendi, On the absorption cross section of CdSe nanocrystal quantum dots, J. Phys. Chem. B **106**, 7619 (2002).

[4] J. Liu, P. Liu, D. Chen, T. Shi, X. Qu, L. Chen, T. Wu, J. Ke, K. Xiong, M. Li, *et al.*, A near-infrared colloidal quantum dot imager with monolithically integrated readout circuitry, Nat. Electron. **5**, 443 (2022).

[5] Y. Kim, *et al.*, A facet-specific quantum dot passivation strategy for colloid management and efficient infrared photovoltaics, Adv. Mater. **31**, 1805580 (2019).

[6] R. H. Gilmore, Y. Liu, W. Shcherbakov-Wu, N. S. Dahod, E. M. Y. Lee, M. C. Weidman, H. Li, J. Jean, V. Bulović, A. P. Willard, *et al.*, Epitaxial dimers and Auger-assisted detrapping in PbS quantum dot solids, Matter **1**, 250 (2019).

[7] B. K. Hughes, J. L. Blackburn, D. Kroupa, A. Shabaev, S. C. Erwin, A. L. Efros, A. J. Nozik, J. M. Luther, and M. C. Beard, Synthesis and spectroscopy of PbSe fused quantum-dot dimers, J. Am. Chem. Soc. **136**, 4670 (2014).

[8] A. Stavrinadis, S. Pradhan, P. Papagiorgis, G. Itskos, and G. Konstantatos, Suppressing deep traps in PbS colloidal quantum dots via facile iodide substitutional doping for solar cells with efficiency >10%, ACS Energy Lett. **2**, 739 (2017).

[9] J. Cui, Y. E. Panfil, S. Koley, D. Shamalia, N. Waiskopf, S. Remennik, I. Popov, M. Oded, and U. Banin, Colloidal quantum dot molecules manifesting quantum coupling at room temperature, Nat. Commun. **10**, 5401 (2019).

[10] Y. Cao, A. Stavrinadis, T. Lasanta, D. So, and G. Konstantatos, The role of surface passivation for efficient and photostable PbS quantum dot solar cells, Nat. Energy **1**, 16035 (2016).

[11] X. Yang, J. Yang, M. I. Ullah, Y. Xia, G. Liang, S. Wang, J. Zhang, H. Hsu, H. Song, and J. Tang, Enhanced passivation and carrier collection in ink-processed PbS quantum dot solar cells via a supplementary ligand strategy, ACS Appl. Mater. Interfaces **12**, 42217 (2020).

[12] J. Z. Fan, N. T. Andersen, M. Biondi, P. Todorovic, B. Sun, O. Ouellette, J. Abed, L. K. Sagar, M. J. Choi, S. Hoogland, F. P. G. de Arquer, and E. H. Sargent, Mixed lead halide passivation of quantum dots, Adv. Mater. **31**, 1904304 (2019).

[13] M. Biondi, *et al.*, Facet-oriented coupling enables fast and sensitive colloidal quantum dot photodetectors, Adv. Mater. **33**, 2101056 (2021).

[14] H. Beygi, S. A. Sajjadi, A. Babakhani, J. F. Young, and F. C. J. M. van Veggel, Surface chemistry of as-synthesized and air-oxidized PbS quantum dots, Appl. Surf. Sci. **457**, 1 (2018).

[15] A. H. Ip, A. Kiani, I. J. Kramer, O. Voznyy, H. F. Movahed, L. Levina, M. M. Adachi, S. Hoogland, and E. H. Sargent, Infrared colloidal quantum dot photovoltaics via coupling enhancement and agglomeration suppression, ACS Nano **9**, 8833 (2015).

[16] Y. C. Li, Z. Wang, T. Yuan, D. Nam, M. Luo, J. Wicks, B. Chen, J. Li, F. Li, F. P. G. de Arquer, *et al.*, Binding site diversity promotes CO_2 electroreduction to ethanol, J. Am. Chem. Soc. **141**, 8584 (2019).

[17] See Supplemental Material at http://link.aps.org/supplemental/10.1103/PhysRevApplied.19.014021. Figures S1(a) and S1(b) show (100) facets' passivation with Br^- and I^- at top site.

[18] P. E. Blöchl, Projector augmented-wave method, Phys. Rev. B **50**, 17953 (1994).

[19] G. Kresse and J. Furthmüller, Efficient iterative schemes for *ab initio* total-energy calculations using a plane-wave basis set, Phys. Rev. B **54**, 11169 (1996).

[20] J. P. Perdew, K. Burke, and M. Ernzerhof, Generalized Gradient Approximation Made Simple, Phys. Rev. Lett. **77**, 3865 (1996).

[21] H. J. Monkhorst and J. D. Pack, Special points for Brillouin-zone integrations, Phys. Rev. B **13**, 5188 (1976).

[22] K. Momma and F. Izumi, VESTA 3 for three-dimensional visualization of crystal, volumetric and morphology data, J. Appl. Crystallogr. **44**, 1272 (2011).

[23] See Supplemental Material at http://link.aps.org/supplemental/10.1103/PhysRevApplied.19.014021. Figures S1(c) and S1(d) show (100) facets' passivation with $10Br^-$ and $10I^-$ at bridge site.

[24] M. Liu, O. Voznyy, R. Sabatini, F. P. G. de Arquer, R. Munir, A. H. Balawi, X. Lan, F. Fan, G. Walters, A. R. Kirmani, *et al.*, Hybrid organic–inorganic inks flatten the energy landscape in colloidal quantum dot solids, Nat. Mater. **16**, 258 (2017).

[25] Y. Xia, S. Liu, K. Wang, X. Yang, L. Lian, Z. Zhang, J. He, G. Liang, S. Wang, M. Tan, H. *et al.*, Cation-exchange synthesis of highly monodisperse PbS quantum dots from ZnS nanorods for efficient infrared solar cells, Adv. Funct. Mater. **30**, 1907379 (2020).

[26] J. Mooney and P. Kambhampati, Get the basics right: Jacobian conversion of wavelength and energy scales for quantitative analysis of emission spectra, J. Phys. Chem. Lett. **4**, 3316 (2013).

[27] See Supplemental Material at http://link.aps.org/supplemental/10.1103/PhysRevApplied.19.014021. Figure S9 shows atomic concentration of Pb, S, Br, I, C, *and*O in films based on XPS.

[28] See Supplemental Material at http://link.aps.org/supplemental/10.1103/PhysRevApplied.19.014021. Table SII shows molar concentration of PbS, $PbBr_2$, and PbI_2 in films based on XPS.

[29] M. Liu, S. D. Verma, Z. Zhang, J. Sung, and A. Rao, Nonequilibrium carrier transport in quantum dot heterostructures, Nano Lett. **21**, 8945 (2021).

[30] See Supplemental Material at http://link.aps.org/supplemental/10.1103/PhysRevApplied.19.014021. Table SI shows detailed PL peak-splitting data of PbS CQD films with different excitation power.

[31] *Advanced Characterization Techniques for Thin Film Solar Cells*, edited by, D. Abou-Ras, T. Kirchartz, and U. Rau (Wiley-VCH Verlag GmbH & Co. KGaA, Weinheim, 2016), Chap. 7.

[32] C. H. M. Chuang, A. Maurano, R. E. Brandt, G. W. Hwang, J. Jean, T. Buonassisi, V. Bulovic, and M. G. Bawendi, Open-circuit voltage deficit, radiative sub-bandgap states, and prospects in quantum dot solar cells, Nano Lett. **15**, 3286 (2015).

[33] See Supplemental Material at http://link.aps.org/supplemental/10.1103/PhysRevApplied.19.014021. Figure S2 shows cross-section SEM image.

[34] See Supplemental Material at http://link.aps.org/supplemental/10.1103/PhysRevApplied.19.014021. Figure S3 shows light and dark J-V curves of the devices passivated by $1 \times PbBr_2$, $4 \times PbBr_2$, $8 \times PbBr_2$, and $16 \times PbBr_2$.

[35] See Supplemental Material at http://link.aps.org/supplemental/10.1103/PhysRevApplied.19.014021. Figure S4 shows the circuit model of the p-n junction.

[36] Q. K. Yang, F. Fuchs, J. Schmitz, and W. Pletschen, Investigation of trap-assisted tunneling current in InAs/(GaIn)Sb superlattice long-wavelength photodiodes, Appl. Phys. Lett. **81**, 4757 (2002).

[37] J. P. Clifford, K. W. Johnston, L. Levina, and E. H. Sargent, Schottky barriers to colloidal quantum dot films, Appl. Phys. Lett. **91**, 253117 (2007).

[38] See Supplemental Material at http://link.aps.org/supplemental/10.1103/PhysRevApplied.19.014021. Figure S5 shows transient absorption (TA) decay of PbS CQD films passivated by $1 \times PbBr_2$ and $8 \times PbBr_2$.

[39] See Supplemental Material at http://link.aps.org/supplemental/10.1103/PhysRevApplied.19.014021. Figure S6 shows color maps of TA.

[40] Y. Yang, W. Rodríguez-Córdoba, and T. Lian, Ultrafast charge separation and recombination dynamics in lead sulfide quantum dot–methylene blue complexes probed by electron and hole intraband transitions, J. Am. Chem. Soc. **133**, 9246 (2011).

[41] Q. Shen, K. Katayama, T. Sawada, S. Hachiya, and T. Toyoda, Ultrafast carrier dynamics in PbS quantum dots, Chem. Phys. Lett. **542**, 89 (2012).

[42] C. Qin, J. Guo, Z. Zhou, Y. Liu, and Y. Jiang, Hot excitons cooling and multiexcitons Auger recombination in PbS quantum dots, Nanotechnology **32**, 185701 (2021).

[43] P. Guyot-Sionnest, Electrical transport in colloidal quantum dot films, J. Phys. Chem. Lett. **3**, 1169 (2012).

[44] J. Tang and E. H. Sargent, Infrared colloidal quantum dots for photovoltaics: Fundamentals and recent progress, Adv. Mater. **23**, 12 (2011).

[45] See Supplemental Material at http://link.aps.org/supplemental/10.1103/PhysRevApplied.19.014021. Figure S7 shows AFM images of films passivated by $1 \times PbBr_2$, $4 \times PbBr_2$, $8 \times PbBr_2$, and $16 \times PbBr_2$.

[46] See Supplemental Material at http://link.aps.org/supplemental/10.1103/PhysRevApplied.19.014021. Figure S8 shows XPS of the main elements (Pb4f, I3d, C1s, O1s, Br3d, S2p orbits).

[47] W. Ahmad, J. He, Z. Liu, K. Xu, Z. Chen, X. Yang, D. Li, Y. Xia, J. Zhang, and C. Chen, Lead selenide (PbSe) colloidal quantum dot solar cells with >10% efficiency, Adv. Mater. **31**, 1900593 (2019).

[48] F. Hetsch, N. Zhao, S. V. Kershaw, and A. L. Rogach, Quantum dot field effect transistors, Mater. Today **16**, 312 (2013).

[49] S. Lu, H. Ding, J. Hu, Y. Liu, J. Zhu, R. Kondrotas, C. Chen, and J. Tang, In situ investigation of interfacial properties of Sb_2Se_3 heterojunctions, Appl. Phys. Lett. **116**, 241602 (2020).

[50] J. P. Clifford, G. Konstantatos, K. W. Johnston, S. Hoogland, L. Levina, and E. H. Sargent, Fast, sensitive and spectrally tuneable colloidal-quantum-dot photodetectors, Nat. Nanotechnol. **4**, 40 (2009).

[51] T. Rauch, M. Böberl, S. F. Tedde, J. Fürst, M. V. Kovalenko, G. Hesser, U. Lemmer, W. Heiss, and O. Hayden, Near-infrared imaging with quantum-dot-sensitized organic photodiodes, Nat. Photonics **3**, 332 (2009).

[52] See Supplemental Material at http://link.aps.org/supplemental/10.1103/PhysRevApplied.19.014021. Figure S9 shows statistics of specific detectivity (D*) of PbS CQD photodetectors reported in previous works and this work.

[53] J. R. Manders, T. H. Lai, Y. An, W. Xu, J. Lee, D. Y. Kim, G. Bosman, and F. So, Low-Noise Multispectral photodetectors made from all solution-processed inorganic semiconductors, Adv. Funct. Mater. **24**, 7205 (2014).

[54] K. Szendrei, F. Cordella, M. V. Kovalenko, M. Böberl, G. Hesser, M. Yarema, D. Jarzab, O. V. Mikhnenko, A. Gocalinska, M. Saba, *et al.*, Solution-processable near-IR photodetectors based on electron transfer from PbS nanocrystals to fullerene derivatives, Adv. Mater. **21**, 683 (2009).

[55] K. Xu, X. Xiao, W. Zhou, X. Jiang, Q. Wei, H. Chen, Z. Deng, J. Huang, B. Chen, and Z. Ning, Inverted Si:PbS colloidal quantum dot heterojunction-based infrared photodetector, ACS Appl. Mater. Interfaces **12**, 15414 (2020).

[56] M. Vafaie, J. Z. Fan, A. M. Najarian, O. Ouellette, L. K. Sagar, K. Bertens, B. Sun, F. P. G. de Arquer, and E. H. Sargent, Colloidal quantum dot photodetectors with 10-ns response time and 80% quantum efficiency at 1,550 nm, Matter **4**, 1042 (2021).

[57] See Supplemental Material at http://link.aps.org/supplemental/10.1103/PhysRevApplied.19.014021. Figure S11 shows PL spectrum and XRD pattern of ZnO film.